Biaxial Nanowrinkling in Cholesteric Surfaces: Egg Carton Surfaces through Chiral Anchoring

Ziheng Wang[1], Phillip Servio[1], Alejandro Rey[1,*]

Abstract

Periodic micro and nano-structured surfaces in nature are responsible for functionalities including structural colour, superhydrophobicity, where wrinkling plays a significant role. The Bouligand architecture of fibrous composites such as insect exoskeleton and plant cell walls has been shown to generate uniaxial single and multiscale nanowrinkling through the chiral capillarity effect due to anisotropic surface tension and the helical fibre arrangement. The helical arrangement in Bouligand structures is a solid analogue of a cholesteric liquid crystal, which is an intermediate stage in the self-assembly formation process of fibrous composites. We extend uniaxial wrinkling predictions to biaxial wrinkling and show, using the liquid crystal shape equation, how and why egg carton surfaces with orthogonal patterning arise, since a planar helix tangential to a surface is unstable to oblique wrinkling modes. Taken together this work contributes to novel surface pattern formation and engineering principles to study surfaces of biological materials.

Keywords: chiral liquid crystals, liquid crystal shape equation, helicoidal plywoods, uniaxial wrinkling, biaxial wrinkling, egg carton surfaces
2010 MSC: 76A15

1. Introduction

Bulk and surface pattern formation is an active area of material research [1, 2], and in this paper the pattern of interest and investigation is the ideal egg car-

*Corresponding author

ton surface [2]; it is noted that a universal egg carton surface nomenclature does not exist at the moment and different disciplines refer to it as concave/convex surfaces [3], sinusoidal surfaces [1] and so-on. Many biological, geological and man-made materials display the egg carton architecture. For example, amphotericin B/deoxycholate on multilamellar vesicles affects the DPPC/cholesterol system, shows egg carton surfaces (the scale is around 50 nm) [3]. A similar egg carton surface structure is found in the didodecanoyl-(PG-LPG) mixture [4]. Egg caron surface also appears on electropolished zirconium (Fig. 1(A)) [5], (Fig. 1(B)) [1], the papillae of red rose petal (Fig. 1(D)) displays a related egg carton [6], even rocks (Fig. 1(E)) [7] subjected to erosion-driven shaping shows cm-scale macroscopic egg cartons. Clearly, shape-functionality relations are expected to be rich and to generate numerous optimal properties, as the egg carton geometry is abundant in the spherical, saddle, and cylindrical patches, leveraging geometric diversity across space, without joining and gluing operations.

Theoretical research on those surfaces was previously performed by using the elastic energy [8] or mean-field theory [9]. In our paper, we proposed a novel linear mechanism for generating egg carton surfaces credit to the minimization of the surface anchoring. Any cholesteric LC compound satisfying our assumption should be able to do such egg carton surface. To practically generate such surfaces, we need to generate a uniform helix structure. The common methods include cooling liquid crystal from the isotropic phase under electric field or mechanical sheering, or with the help of the polymer network in the bulk for stabilization [10], even with the presence of UV light [11].

Biological fibrous composites, such as cellulose in plant cell walls, chitin in arthropods cuticles, and collagen in human compact bones, use Bouligand's twisted plywood architecture, known as liquid crystal analogue which is similar to that of cholesteric liquid crystal (CLC), shown in Figure 2(a) [12, 13, 14, 15, 16, 17, 18, 19, 20, 21, 22, 23, 24, 25, 26, 27]. The structure of a CLC is defined by the helix axis $\hat{\mathbf{C}}$ (unit vector), the pitch length P_0 required for a 2π rotation, and handedness (sign of P_0), and the average fibre orientation or director $\mathbf{n}$ which is normal to $\hat{\mathbf{C}}$. Since $\mathbf{n}$ is a unit vector, its gradient is normal to $\mathbf{n}$ ($\mathbf{n} \cdot \nabla \mathbf{n} = 0$)

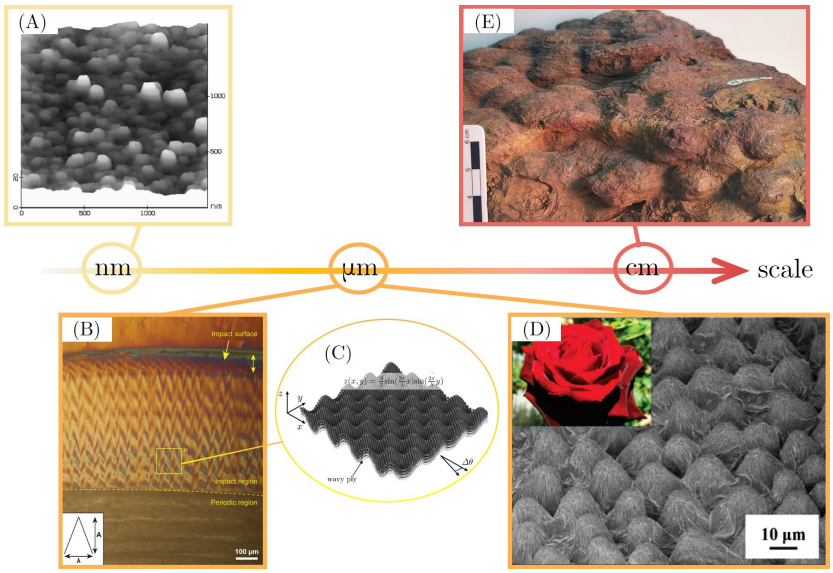

Figure 1: A schematic summarizing the ubiquitous egg carton structures exhibiting in different materials: (A) AFM image of the egg carton surface of zirconium electropolished at 70 V. Adapted from [5], with the permission of AIP Publishing (©1999 AIP Publishing). (B) Differential interference contrast image of the dactyl club from *Odontodactylus scyllarus*. Adapted from [1], with the permission of John Wiley & Sons (©2016 John Wiley & Sons). (C) Herringbone-Bouligand structure in (B) and the equation used to capture the surface properties. Adapted from [2], with the permission from Elsevier (©2020 Elsevier). (D) SEM image of a red rose petal surface. Adapted with permission from [6] (©2008 American Chemical Society). (E) The egg carton surface of the organosedimentary structure of stromatolites [7]. Adapted from [7], with the permission from Springer Nature (©2020 Springer Nature).

but for a chiral cholesteric its helicity $B = \mathbf{n} \cdot \nabla \times \mathbf{n} = 2\pi/P_0 \neq 0$ [13]. Directed chiral nematic liquid crystal (CLC) self-assembly is the formation mechanism of these biological structures, as demonstrated through defect generation phenomena [28, 29, 30, 31]. Discussions of the intimate correspondence between LCs and biological plywoods [13] show that LC theories offer a route for biomimetic process engineering of advanced materials [13] and also can shed light on biological processes such as morphogenesis [32], and the optimal material functionalities such as structural colour [33], super-hydrophobicity, tribology, drag reduction, self-healing and more [12, 13, 34, 35, 36]. More recently validated modeling

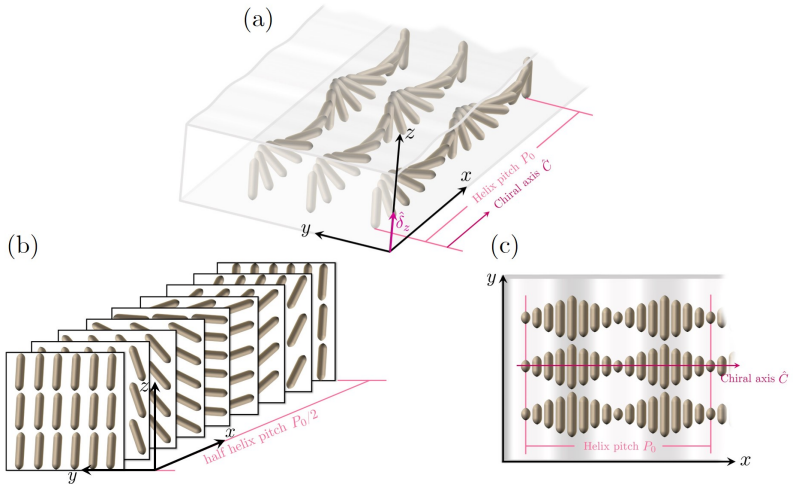

Figure 2: (a) 3-D schematic of a cholesteric fibre architecture, where the rods denote the average fibre orientation; moving along "x" the rods rotate continuously, say clockwise, defining the pitch $P_0 = 2\pi/q_0$ or distance for a full 2π rotation of the average fibre orientation $\mathbf{n}$ (unit vector or director); here q_0 is the cholesteric wave-vector. (b) The director $\mathbf{n}$ is a constant on each (y, z)-slices, showing the layered organization of cholesterics. (c) 2-D planar view ((x, y)-plane) of the cholesteric helix whose chiral axis $\hat{\mathbf{C}}$ is along the x-direction and $\hat{\boldsymbol{\delta}}_z$ is the outward surface unit normal along the z-direction. For a uniform planar helix $\hat{\mathbf{C}} \cdot \hat{\boldsymbol{\delta}}_z = 0$.

based on LC physics for material synthesis and processing of cholesteric collagen shows that aqueous lyotropic cholesterics offer efficient pathways for engineering biomimetics [37, 38, 39].

A significant issue in LC-based biomimetic engineering is whether liquid crystal self-assembly is capable to generate surface architectures with micron and nanoscale features as found in many natural materials. At the simplest geometric level, folding, wrinkling and creasing are three fundamental surface features, recognized as building blocks for various functionalities [40, 41, 42]. In particular single and dual scale wrinkling has been shown to generate structural colours. The petals of many floral plants have remarkable optical properties, such as iridescence and a striking metallic appearance. Structural colour in flowers, such as the iridescence exhibited by *Hibiscus trionum* and *Tulipa kaufmanniana* petals is determined by surface diffraction gratings that consist of

ordered striations or ridges that form on the epidermal cells [43]. These uniaxial wrinkling generate so-called cylindrical surfaces, since they only display curvature in a single direction. Many other examples from nature indicate biaxial wrinkling as in the egg carton surface where there are two orthogonal wrinkling wave-vector creating peaks and valleys in two directions, which are expected to enhanced properties through more additional symmetry breaking.

Mechanisms for surface pattern formation in membranes and surfaces are usually classified into elastic and/or anchoring instabilities [40, 42]. The elastic mechanism usually involve applied compressional stress and material property mismatch between surface and substrate. Anchoring is a surface pattern formation mechanism arising only from anisotropic surface tension and is found in both crystals and liquid crystals [44]. The relation between crystal and liquid crystal surface pattern formation mechanisms has been established by considering the capillary vector and notably LCs usually display another mode called the director capillary pressure because $\mathbf{n}$ is a variable on the surface and is not a fixed structural feature [44, 45, 46]. LC surface anchoring has been shown to generate the same wrinkling and creasing patterns without the application of compressive external stress. This intrinsic LC mechanism only depends on the anisotropic contribution $W(\mathbf{n}(x)\cdot\mathbf{k})^2/2$ to the space-dependent surface tension $\gamma(x)$ [44]:

$$\gamma(x) = \gamma_0 + \frac{W}{2}(\mathbf{n}(x)\cdot\mathbf{k})^2 \tag{1}$$

were γ_0 is the isotropic surface tension, W is the chemical composition/temperature dependent anchoring constant and $\mathbf{k}$ is the surface unit normal. Since for most known cases $|W|/\gamma_0 \ll 1$ anchoring creates wrinkles of nanoscale amplitude and since the spatial scale of $\mathbf{n}$ is the pitch P_0, the wave-length of the wrinkles is in the micron-range. The sign of W determines the minimum energy of anchoring: $W > 0$ is for tangential orientation and $W < 0$ for perpendicular and only controls the up-down orientation of peaks and valleys; symmetry relations are discussed in [47]. Higher order terms such as $(\mathbf{n}\cdot\mathbf{k})^4$ are important to generate more surface symmetry breaking and secondary surface wrinkling [47, 48, 49].

Since $\mathbf{n}$ represents the structure and $\mathbf{k}$ the geometry, the surface energy is tunable (spatial increase or decrease) by changing the fibre orientation $\mathbf{n}$, changing the surface orientation $\mathbf{k}$, changing the surface area or all the above, capable of generating a rich surface pattern formation landscape. For uniaxial wrinkling it was found that director capillary pressure ($\propto \nabla_s \mathbf{n}$) is the driving force and the Laplace pressure ($\propto \nabla_s \cdot \mathbf{k}$) due to curvature is the resistance; here ∇_s is the surface gradient operator. It is noted that the anchoring mechanism was used to describe the LC Plateau-Rayleigh fibre instability in achiral nematic LCs, which includes surface wrinkling and twisting modes observed experimentally in collagen solutions. Consistency of the anchoring driven surface patterning predictions with experimental observations [50, 51, 52, 53, 54] of surface pattern formation include: (1) scaling laws for single wrinkling in cholesteric surfaces [47]; (2) scaling laws for two scale wrinkling in cholesteric surfaces [48, 49]; (3) tribological enhancement as a function of surface patterns' moments [47]; (4) optical gratings from chiral anchoring [33].

All these previous predictions [33, 47, 48, 49] and observations focus on uniaxial wrinkling in LCs, with one single wrinkling wave vector and for cases where the helix is uncoiled; in this paper the helix is intact and undeformed. The important issue considered in this paper is whether this well-established mechanism of chiral anchoring instabilities is able to capture biaxial wrinkling as in egg carton surfaces [55, 56, 57] without the complexity of high order elastic membrane models [56, 57] used to capture these biaxially wrinkled surfaces. Understanding this pattern and their modifications can be used to explain nature's more complex surfaces and generate surface structures with biaxial functionality, beyond the simple single wrinkling. Hence we start this investigation of multiple wave-vector wrinkling using the simplest possible linear model with minimal assumptions and focus solely on the egg carton geometry with biaxial wrinkling of an initially uniformly aligned cholesteric LCs, known as uniformly aligned helix (ULH) parallel to the surface [58, 59, 60], as shown in Figure 3. The issue is whether and how a flat surface with a uniform tangentially aligned helix decays into an egg carton surface and what is the most likely orientation

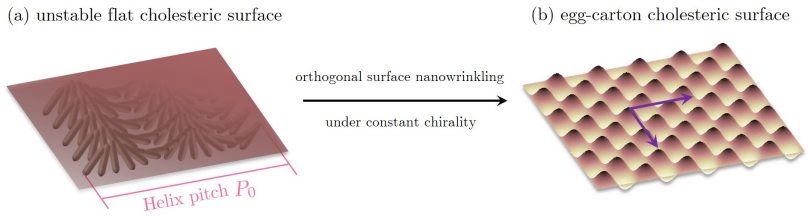

Figure 3: Schematic of the key question addressed in this paper: is the initial flat surface layer (a) of a uniform cholesteric liquid crystal of pitch P_0 unstable to director pressure due to chiral anchoring such that the instability produces the symmetric ideal egg carton surface (b) with equi-biaxial wrinkling?

of the wrinkling frame with respect to the $\hat{\mathbf{C}}$ axis.

The particular objectives of this paper are:

1. Establish the mechanism of biaxial wrinkling that leads to egg carton surfaces in undeformed ideal cholesteric liquid crystals;
2. Characterize the egg carton surfaces in terms of amplitude/wave-length relations;
3. Identify the role of anchoring constant and cholesteric pitch in biaxial wrinkling.

2. Methodology

To achieve these objectives this paper focuses on principles and mechanisms and physical predictions and only presents the necessary and sufficient mathematical details. We briefly rationalize our assumptions and give quantitative estimates of the relative importance of neglected effects, as follows.

1. Bulk flow is neglected because we consider interfacial patterns formation in a cholesteric liquid crystalline polymer and as such the relevant dimensionless number that governs the ratio of flow to elastic effects, known as the Ericksen number E is essentially negligible:

$$\text{Ericksen number: } E = \frac{\text{Flow Effect}}{\text{Bulk Elasticity Effect}} = \frac{\eta \dot{D} P_0^2}{K}$$

where η is a characteristic viscosity, $\dot{D}$ is a deformation rate, P_0 is the pitch, and K is the Frank elastic constant (see for example, [61, 12, 62, 26]). In the present process, there is no imposed external flow, and the deformation rate $\dot{D}$ can only arise from weak back-flow effects, that is internal re-orientation driven relaxation. Using typical quantities (see for example, [63, 12])

$$\eta \approx 100\text{Pas}, \quad \dot{D} \approx 10^{-3}\text{s}^{-1}, \quad P_0 \sim 10^{-6}\text{m}, \quad K \sim 10^{-11}\text{N} \rightarrow E \sim 10^{-2} \ll 1$$

To observe significant flow effects the E number should be grated than 10-100 and for that one need imposed external flows. Another important fact that diminishes the presence of flow effects during the egg carton formation is the presence of ultra-high viscosity permeation flow (see for example, [64, 65]). In cholesteric liquid crystals, flow along or close to the helix axis is essentially blocked by the presence of ultra high viscosity; the only "liquid-like" low viscosity directions are along the normal planes to the helix and since in our case the potential flow has to be tangential to the surface and along the helix axis, we conclude that its magnitude will be essentially negligible. In partial summary, nematorheology [62], provides a foundation to make the insignificant bulk-flow assumption.

2. Bulk elasticity: The complete shape equation is the projection of normal stress interfacial jump (see for example, [44]). The liquid crystal shape equation includes the bulk elasticity (Frank elasticity) contribution arising from orientation gradients at the interface and this effect is known as the "elastic correction". The relative importance of the bulk elasticity compared to the isotropic surface tension effects is the elasticity ratio R:

$$\text{Elastic Ration: } R = \frac{\text{Bulk Elastic Effect}}{\text{Surface Tension Effect}} = \frac{K}{P_0\gamma_0}$$

Using characteristic values (see for example, [12, 66]) we estimate that $R \ll 1$:

$$\gamma_0 \sim 5 \times 10^{-2}\text{N/m}, \quad P_0 \sim 10^{-6}\text{m}, \quad K \sim 10^{-11}\text{N} \rightarrow R \sim 10^{-4} \ll 1$$

The essentially insignificant "eleastic correction" ($R \ll 1$) was discussed in [33].

3. Transport effects: We consider isothermal conditions with no temperature gradients. We consider a stable thermodynamic lyotropic cholesteric liquid crystalline phase far from any biphasic gap in the phase diagram (see for example, [67]). This thermodynamic stable condition is achievable by sufficiently high concentration such that the Onsager liquid crysal transition concentration (see for example, [12]) is achieved. For long rods this is easily achievable and that is why we observed these anisotropic phases when molecular anisotropy (molecular persistence length/effective molecular diameter) is high.
4. Marangoni flow: Tangential (to the surface) Marangoni flows in nematic liquid crystals can arise not only from thermal and/or concentration gradients (not present in our case) but also from gradents in director orientation and gradients in molecular order parameters (see for example, [68]). As explained in 1., the tangential flows are blocked by the permeation effect and hence tangential Marangoni flow can not play a significant effect in egg carton formation.
5. Complex anchoring models: In this paper we use the simplest quadratic anchoring model (Eqn. (1)), consistent with the objectives of this work. Fourth and higher order models were explored in our previous work [47] and are expected to introduce complex variants in the ideal egg carton, such as multiscale egg cartons. These will be explored in the future.
6. Spatial pitch gradients: These may arise when there are externally imposed concentration gradients or under phase separation. In this work there are no externally imposed concentration gradients (no diffusional Marangoni flow) and only a stable single phase liquid crystal. The net impact of a concentration gradient is to change the pitch length and if that would be present then the egg carton peak-to-peak distance may change as well as its amplitude, since larger pitch leads to a larger amplitude in surface distortions. These effects were explored in [33], in the context of

single wrinkling.

7. Transient modes: This paper concentrates on statics and the instability mechanism that leads to time-independent egg cartons shapes. As such time evolution is not part of the model and the temporal evolution is not in the scope of this work. To capture the transient evolution the dynamic versions of the shape equation coupled with the interfacial and bulk torque and momentum balance equations need to be considered. Steady state, static, and equilibrium pattern formation models provide information on instability mechanisms and driving forces.

In this paper we analyze nano-wrinkling of homogeneous cholesteric liquid crystals whose chiral axis $\hat{\mathbf{C}} = \hat{\boldsymbol{\delta}}_x$ is aligned parallel to an initially flat surface with a unit normal $\mathbf{k}^0 = \hat{\boldsymbol{\delta}}_z$ in rectangular coordinates (x, y, z), with chiral vector $\mathbf{q} = q\hat{\boldsymbol{\delta}}_x$, pitch P_0, and director field $\mathbf{n}(\mathbf{q}\cdot\mathbf{r}) = \begin{bmatrix} 0 & \sin\theta & \cos\theta \end{bmatrix}^T$, director angle $\theta = \mathbf{q}\cdot\mathbf{r} = qx$, $q = 2\pi/P_0$, $\mathbf{q} = q\hat{\boldsymbol{\delta}}_x$, $\mathbf{r} = x\hat{\boldsymbol{\delta}}_x + y\hat{\boldsymbol{\delta}}_y + x\hat{\boldsymbol{\delta}}_z$. The LC shape equation, under zero bulk stress jump condition is a balance of three pressures [44, 46, 47]:

$$0 = \underbrace{\gamma_0(\kappa_1+\kappa_2)}_{\text{Laplace pressure}} \underbrace{+W\left(((\mathbf{n}\cdot\mathbf{e}_1)^2-(\mathbf{n}\cdot\mathbf{k})^2)\kappa_1+((\mathbf{n}\cdot\mathbf{e}_2)^2-(\mathbf{n}\cdot\mathbf{k})^2)\kappa_2\right)}_{\text{Helfrich pressure}}$$
$$\underbrace{-W\left((\mathbf{n}\cdot\mathbf{k})\nabla_s\cdot\mathbf{n}+\mathbf{k}\mathbf{n}:\nabla_s\mathbf{n}\right)}_{\text{Director pressure}} \tag{2}$$

Here κ_1 and κ_2 are the principal curvatures, $\mathbf{e}_1$ and $\mathbf{e}_2$ are the principal directions. Using standard asymptotic expansion with respect to the small parameter $\epsilon = W/\gamma_0$, all quantities read:

$$\gamma = \gamma_0+\epsilon\gamma^1+\ldots; \quad \mathbf{k} = \mathbf{k}^0+\epsilon\mathbf{k}^1+\ldots; \quad \nabla_s = \nabla_s^0+\epsilon\nabla_s^1+\ldots; \quad \kappa = \kappa^0+\epsilon\kappa^1+\ldots$$

The zero order of all geometric quantities are independent of curvature, such that $\mathbf{k}^0 = \hat{\boldsymbol{\delta}}_z$, $\nabla_s^0 = \hat{\boldsymbol{\delta}}_x\frac{\partial}{\partial x} + \hat{\boldsymbol{\delta}}_y\frac{\partial}{\partial y}$ and so on. The second term (area rotation) in Eqn. (2) is proportional to $-\frac{\partial}{\partial\mathbf{k}}(\mathbf{I}_s\cdot\frac{\partial\gamma}{\partial\mathbf{k}}):\nabla_s\mathbf{k}$, which vanishes under the first order approximation $\mathbf{k} = \mathbf{k}^0$. The linear shape equation now reads:

$$\kappa_1^0+\kappa_2^0 = \epsilon\left((\mathbf{n}\cdot\mathbf{k}^0)\nabla_s^0\mathbf{n}+\mathbf{k}^0\mathbf{n}:\nabla_s^0\mathbf{n}\right) \tag{3}$$

Eqn. (3) shows that the stationary average curvature will be nonzero $(\kappa_1^0 + \kappa_2^0)/2 \neq 0$ if the director pressure is not zero, $\epsilon\left((\mathbf{n}\cdot\mathbf{k}^0)\nabla_s^0\mathbf{n} + \mathbf{k}^0\mathbf{n} : \nabla_s^0\mathbf{n}\right) \neq 0$, a condition easily found under surface orientation gradients.

To achieve the objectives mentioned above we implement the following sequential procedure:

1. (Sec. 3.1) to start we find surface relief $h^+(x')$ solutions along an arbitrary wrinkling wave vector $\mathbf{w}(\alpha)$ in the direction x', of angle $0 \leq \alpha \leq \pi/2$ (or equivalently $\pi \leq \alpha \leq 3\pi/2$) with respect to the x-axis;
2. (Sec. 3.2) use symmetry to find the corresponding surface relief solution $h^-(y')$ corresponding to an orthogonal wave vector $\mathbf{w}(\alpha - \pi/2)$;
3. (Sec. 3.3) use superposition to find biaxial wrinkling $h^B(\alpha, x', y') = h^+(x') + h^-(y')$;
4. (Sec. 3.4) set $\alpha = \pm\pi/4$ and find the symmetric egg carton equi-biaxial solution: $h^{EC} = h^B(\alpha = \pi/4, x', y')$. To avoid redundant repetitions we only emphasize equivalent structures (say $\mathbf{w}$ and $-\mathbf{w}$) obtained from simple π rotations around the z-axis when necessary. The expected up-down symmetry of the surface profiles with respect to the sign of the anchoring W and the sign of the pitch was discussed in previous work [47] and will not be discussed in this paper.

3. Results and Discussion

Next we follow the scheme 1–4 specified above, first establishing the wrinkling mechanism and then predicting egg carton surfaces.

3.1. Chiral anchoring uniaxial wrinkling mechanism and surface relief

We first seek wrinkling solutions along an arbitrary direction x', at an angle α from the x-axis; this wrinkling solutions are plane-wave solutions to the shape Eqn. (3). Figure 4(a) shows the orthogonal (x', y')-axes (wrinkling coordinates) and its relation to the (x, y)-axes (cholesteric material coordinates).

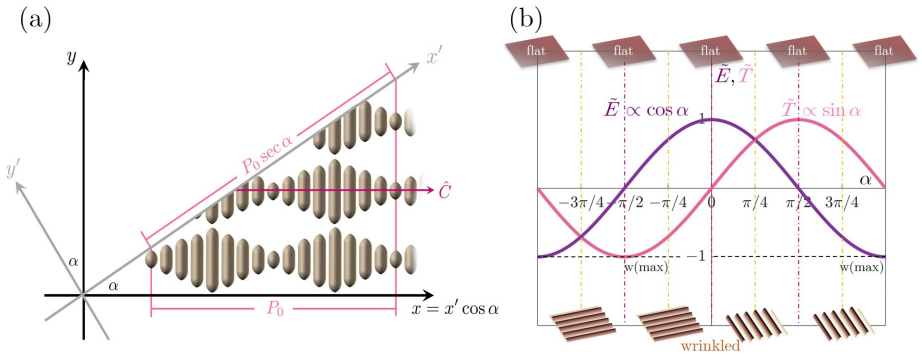

Figure 4: (a) Relations between the cholesteric material coordinates (x, y, z) and the wrinkling coordinates (x', y', z). The angle α defines the wrinkling direction. In material coordinates the director is a pure twist ($n_x = 0$) and is a two component vector but in wrinkling coordinates the director has three components (nx', ny', nz). This follows from a simple clockwise rotation: $[x', y'] = \mathbf{R}(\alpha)[x, y]$, where $\mathbf{R}(\alpha)$ is the rotation matrix. (b) Scaled energy transfer function $\tilde{T}(x' = 0) = \sin\alpha$ and scaled energy input $\tilde{E}$; see Eqn. (5). Since curvature is given by $\kappa = T \cdot E$, its magnitude at $x' = 0$ is maximal at $\alpha = +\pi/4$. This result applies for any x'.

The $x' = x/\cos\alpha$ direction corresponds to the wrinkling wave vector $\mathbf{w}(\alpha)$
195 and the $x = x'\cos\alpha$ direction corresponds to the chiral axis. In material coordinates the director is a pure twist ($n_x = 0$) and is a two component vector but in wrinkling coordinates the director has three components $(n_{x'}, n_{y'}, n_{z'})$. The orientation periodicity in wrinkling coordinates has expanded to $P_0/\cos\alpha$.

In wrinkling (x', y') coordinates the phase angle θ, director $\mathbf{n}'$, and wavevector $\mathbf{w}$ read:

$$x = x'\cos\alpha, \quad w = q\cos\alpha, \quad \theta = \left(\frac{2\pi\cos\alpha}{P_0}\right)x' = wx'$$
$$\mathbf{w} = w\hat{\boldsymbol{\delta}}_{x'}, \quad \mathbf{n}'(x') = -\sin\alpha\sin\theta\hat{\boldsymbol{\delta}}_{x'} + \cos\alpha\sin\theta\hat{\boldsymbol{\delta}}_{y'} + \cos\theta\hat{\boldsymbol{\delta}}_{z'} \tag{4}$$

and the shape Eqn. (3) in terms of the surface relief $h^+(x')$ (where first order term is neglected due to small wrinkling effect) for uniaxial wrinkling in the x'-direction is:

$$\kappa_1^0 = h^+_{x'x'} = -\epsilon w\sin\alpha\cos 2wx' = -\underbrace{\sin\alpha\cos 2wx'}_{T(x',\alpha)}\underbrace{\epsilon q\cos\alpha}_{E(\alpha)} \tag{5}$$

where $T(x', \alpha)$ is the energy transfer function and $E(\alpha)$ is the scaled chiral energy input. Hence to produce wrinkling both T and E must be non-zero. When $\alpha = 0$ the transferable chiral energy content E along x-axis is maximal (full twist along x) and when $\alpha = \pi/2$ it is zero since θ is a constant (achiral direction, and no twist along y-axis; see also Fig. 2(b)). Correspondingly, the energy transfer function $T(x', \alpha)$ is zero and maximal at those two angles.

Figure 4(b) shows the scaled $T(x' = 0, \sin\alpha)$ and $E(\cos\alpha)$ as a function of α that explains why we observe anchoring driven wrinkling for $\alpha \neq 0$, $\pm\pi/2$, $\pm\pi$. Since the curvature is the product of $T \cdot E$, its magnitude is maximal at $\alpha = \pi/4$ and zero at $\alpha = 0$, $\pm\pi/2$, $\pm\pi$, since T is a function of $\sin\alpha$ and E is a function of $\cos\alpha$.

Integrating twice the curvature Eqn. (5), the surface relief $h^+(x')$ is

$$h^+(x') = \frac{\epsilon}{4w}\sin\alpha\cos 2wx' = K + \frac{\sin\alpha}{\gamma_0 w}\left(\frac{W}{2}\cos^2 wx'\right), \quad K = -\frac{\epsilon}{4q}\tan\alpha \quad (6)$$

where K is an unimportant vertical shift. Eqn. (6) is rewritten as a transparent energy balance:

$$\underbrace{\gamma_0 h^+(x')w}_{\text{wrinkling capillary energy}} = \gamma_0 h^+(x') q\cos\alpha$$
$$= \left(\frac{W}{2}\cos^2 wx'\right)\sin\alpha = \underbrace{\gamma_{\text{an}}\sin\alpha}_{\text{transferable anchoring energy}} \quad (7)$$

In any direction x', the transferable anchoring energy $\gamma_{\text{an}}\sin\alpha$ is converted to the wrinkling capillary energy $\gamma_0 h(x')w$. The scaling law for wrinkle amplitude $A(\alpha)$ and wrinkle-wave-length $\lambda'(\alpha)$ is:

$$A(\alpha) = \frac{\epsilon}{2w}\sin\alpha = \left(\frac{\epsilon\sin\alpha}{4\pi}\right)\lambda', \quad \lambda' = \frac{P_0}{\cos\alpha} \quad (8)$$

For a given direction the amplitude A is linear function of the wrinkling wave-length $\lambda' > P_0$, which is larger than the pitch. The former is consistent with our previous results [47, 48, 49] based on uncoiled helices at the surface. In the material coordinate system (x, y, z) the surface profile (Eqn. (6)) now reads:

$$h^+(x, y, \alpha) = \frac{\epsilon\tan\alpha}{4q}\cos(2q\cos\alpha(x\cos\alpha + y\sin\alpha)) \quad (9)$$

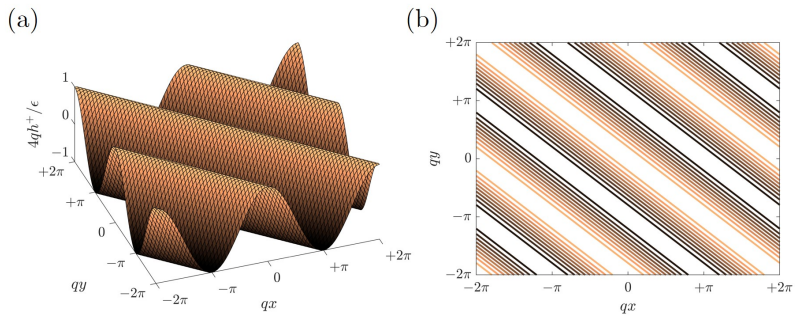

Figure 5: (a) Oblique dimensionless uniaxial wrinkling $4qh^+(x, y, \alpha = \pi/4)/\epsilon$ in the (x, y)-plane and (b) contour plot (a set of lines such that $x + y =$ constant).

Since uniaxial wrinkling is a plane wave it obeys the Helmholtz equation: $\nabla_s^2 h^+ = -(2q\cos\alpha)^2 h^+$, with eigenvalue $(2q\cos\alpha)^2$. Hence the wave number of this equation is $2q\cos\alpha = 2\pi/(P_0 \sec\alpha)$ (Fig. 4(a)). Eqn. (9) is also invariant to the sign of a π-rotation ($\alpha \to \alpha - \pi$) such that solutions for the I and III quadrants give the same result. For the maximal wrinkling curvature conditions at $\alpha = \pm\pi/4$, applicable for both I and III quadrant, we finally find from Eqn. (9) a surface relief in material coordinates:

$$h^+(x, y) = \frac{\epsilon}{4q}\cos(q(x + y)) = \frac{\epsilon}{4q}\left(n_z \cos qy - n_y \sin qy\right) \tag{10}$$

which gives the relation between $h^+(x, y)$ and $\mathbf{n}$; for $y = 0$, $h^+(x, y = 0) = (\epsilon/4q)n_z(x)$ and for $x = 0$, $h^+(x = 0, y) = (\epsilon/4q)\cos qy$.

Figure 5 shows $4qh^+(x, y, \alpha = \pi/4)/\epsilon$ as a function of (x, y) for $q = 1$. The oblique folding to the chiral direction has a periodicity and amplitude described by Eqn. (8).

3.2. Uniaxial wrinkling for orthogonal wave-vectors

Here we describe surface patterning for a wrinkling wave vector that is orthogonal to the case in Sec. 3.1. Using an identical procedure as in Sec. 3.1, simple symmetry rules, and $\alpha \to \alpha - \pi/2$ for a direction corresponding to $-y'$ (see Fig. 4(a); IV quadrant), the uniaxial wrinkling in material coordinates for

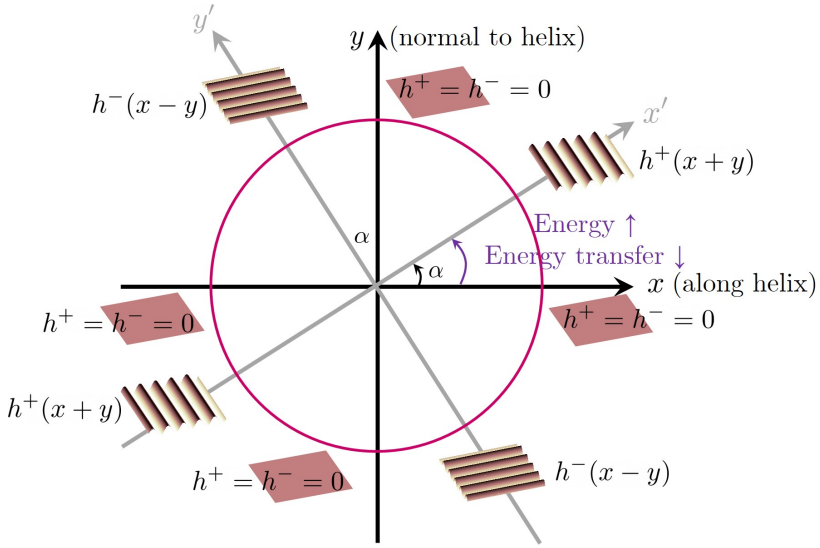

Figure 6: Wrinkling diagram as a function of wrinkling wave vector angle α. The x- and y-axes correspond to flat surfaces and the $\alpha = \pm\pi/4$ lines corresponds to maximal wrinkling curvatures. By symmetry α and $\alpha \pm \pi$ give same wrinkling patterns.

this direction reads:

$$h^-(x,y) = -\frac{\epsilon \cot\alpha}{4q} \cos(2q \sin\alpha (x \sin\alpha - y \cos\alpha)) \tag{11}$$

Eq. (11) is also invariant to a π-rotation ($\alpha \to \alpha - \pi$) and again the II and IV quadrants give same result. Comparing the results between Eqn. (11) and Eqn. (10) we see that an orthogonal wrinkle in the IVth quadrant only interchanges sines and cosines. Again, maximal curvature wrinkles in y' direction give:

$$h^-(x,y) = -\frac{\epsilon}{4q} \cos(q(x-y)) = -\frac{\epsilon}{4q} \left(n_z \cos qy + n_y \sin qy\right) \tag{12}$$

Figure 6 shows a schematic of the uniaxial wrinkled surfaces $h^\pm$ as a function of wrinkling wave-vector directions. The x- and y-axes correspond to flat surfaces where both solutions are equal to zero. For wrinkling wave vectors away from the flat surfaces axes, wrinkling sets in in the (I, III) and (II, IV) quadrants.

3.3. Biaxial wrinkling by superposition orthogonal wave-vectors

To find biaxial wrinkling reliefs $h^B(x,y)$ we use the superposition of the two orthogonal uniaxial wrinkling modes (Eqn. (9) and Eqn. (11)) and obtain:

$$\begin{aligned} h^B(x,y) &= h^+(x,y) + h^-(x,y) \\ &= \frac{\epsilon \tan\alpha}{4q} \cos(2q\cos\alpha(x\cos\alpha + y\sin\alpha)) \\ &\quad - \frac{\epsilon \cot\alpha}{4q} \cos(2q\sin\alpha(x\sin\alpha - y\cos\alpha)) \end{aligned} \tag{13}$$

Again, maximal curvatures are obtained at $\alpha = \pm\pi/4$ but choosing other angles gives rise to more complex wrinkling bidirectional patterns of different wavelengths and amplitudes. Also the sign of the superposition can only shift the structure in the (x,y)-plane and for convenience we pick plus in Eqn. (13).

3.4. Egg carton surfaces and equi-biaxial wrinkling

Finally, to obtain the classical, symmetric equi-biaxial egg carton surfaces $h^{EC}(x,y)$ we specify $\alpha = \pm\pi/4$ in $h^B(x,y)$ (Eqn. (13)) and get

$$h^{EC} = h^+ + h^- = \frac{\epsilon}{4q}\cos(q(x+y)) - \frac{\epsilon}{4q}\cos(q(x-y)) = -\frac{\epsilon}{2q}\sin qx \sin qy \tag{14}$$

Equi-biaxial wrinkling also follows the Helmholtz equation for superposed orthogonal planar waves: $\nabla_s^2 h^{EC} + (\sqrt{2}q)^2 h^{EC} = 0$.

A schematic of the superposition $h^{EC}(x,y) = h^+(x,y) + h^-(x,y)$ is shown in Figure 7; since π rotations do not change wrinkling, the sign of the superposition is immaterial.

Fig. 8 shows in detail the egg carton surface relief $h^{EC}(x,y)$ where the lines of zero curvature or straight lines are $x = y = 0$. The Gaussian curvature K and the mean curvature H of this egg carton surface are:

$$\begin{aligned} H &= -\frac{q\epsilon^3}{16 g^{3/2}} \sin qx \sin qy \left(\cos^2 qx + \cos^2 qy + \frac{8}{\epsilon^2} \right) \\ K &= -\frac{(\epsilon q)^2}{4g^2} \cos(q(x-y)) \cos(q(x+y)) \end{aligned} \tag{15}$$

where the surface metric $g = 1 + \epsilon^2(1 - \cos 2qx \cos 2qy)/8$. For small wrinkling ($h \ll P_0$) we have $g \approx 1$. The deviatoric curvature D is computed by $D =$

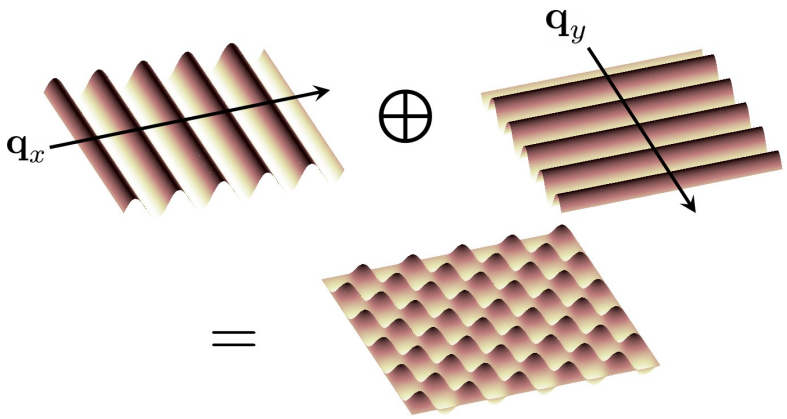

Figure 7: Superposition of orthogonal uniaxial wrinkling leads to a surface with biaxial wrinkling.

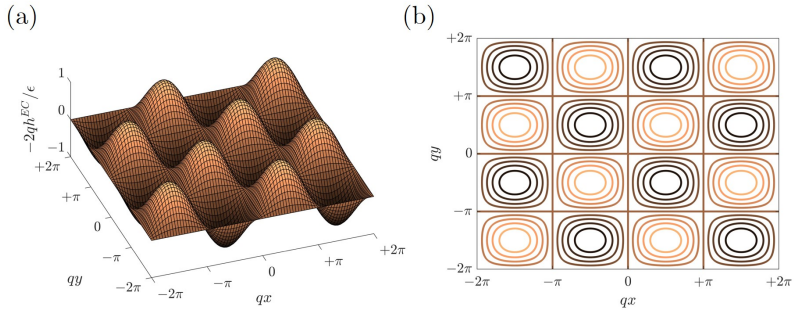

Figure 8: Superposition of two uniaxial wrinkling surfaces at gives the classical egg carton surface (a): $2qh^{EC}/\epsilon = \sin qx \sin qy$. (b) Contour plot of (a) showing a rich periodicity in saddles and spherical points.

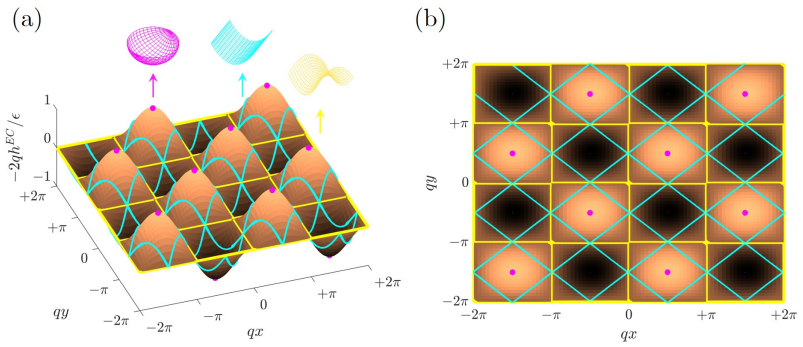

Figure 9: The special patches follow certain patterns on the egg carton surface. (a) The locations of special surface patches mapping on the egg carton surface and (b) is the top view of (a).

$\sqrt{H^2 - K}$. Eqn. (15) shows that the mean curvature and Gaussian curvature distributions are related to both dimensionless anchoring coefficient ϵ and helix pitch $P_0 = 2\pi/q$. The local spherical points ($D = 0$) on the egg carton are located along the half-integer π values of dimensionless coordinates (qx, qy), the saddles ($H = 0$) are located at integer values of π, and the cylinders are along characteristic lines $q(x - y)$ or $q(x + y)$ equal to half-integer values of π. These important results are summarized as follows (n and m are integers):

1. Saddle: vanishing mean curvature ($H = 0$) at $qx = n\pi$ or $qy = m\pi$;
2. Cylinder: vanishing Gaussian curvature ($K = 0$) at $q(x \pm y) = (n + 1/2)\pi$;
3. Sphere: vanishing deviatoric curvature ($D = 0$) at $qx = (n + 1/2)\pi$ and $qy = (m + 1/2)\pi$.

Again the amplitude and wave length follow Eqn. (8); stronger anchoring increases linearly the amplitude. And the summary is visualized in Fig. 9, where the cylinder patches, sphere patches and saddle patches are represented by cyan, yellow and magenta curves or points. The egg carton surface generates rich geometric curvature distribution, thus it is promising to create novel multifunctionalities.

4. Conclusions

In summary, in this paper we have predicted and characterized equi-biaxial wrinkling (egg carton surface) in cholesteric surfaces when the helix axis is initially tangential to the interface. The novel mechanism is due to chiral anchoring of an initially tangentially aligned helix. The previous predictions on the generation of egg carton surface are based on a highly nonlinear elastic model, the Landau-Ginzburg dynamics equations [69] or inclusions with an anisotropic spontaneous curvature [70]. In this paper, we have shown that a simple chiral anchoring-driven surface instability leads to egg carton surfaces with biaxial wrinkling and periodic saddles, which shows a universality for the appearance of the egg carton surface without introducing highly nonlinear elasticity or dynamics. Wrinkling wave vector obliquely aligned to the cholesteric axis can transform anchoring energy into capillary wrinkling. The maximal curvatures of the wrinkles are observed at $\alpha = \pm\pi/4$ from the chiral axis. The wrinkle's amplitude is proportional to the pitch of the helix and to the anchoring constant. The wrinkle's wave-length is proportional to the chiral pitch and to the secant of the wave vector angle. Symmetry principles show that two orthogonal wrinkles with maximal curvature interact to produces the classical egg carton surface. The novel linear mechanism presented here augments previous predictions on generation of egg carton surfaces based on highly nonlinear elastic models [56]. In summary we have shown that a simple chiral anchoring driven surface instability leads to egg carton surfaces with biaxial wrinkling and periodic saddles. These results contribute to the development of new routes of biomimetic surface engineering by using chiral anisotropic soft matter precursors materials that exhibit the ubiquitous Bouligand architecture found throughout nature.

5. Acknowledgement

This work is supported by a grant from the Natural Science and Engineering Research Council of Canada (NSERC Discover Grant, No. 223086). ADR is grateful for financial support through the James McGill Professorship program

at McGill University. ZW is grateful to the Faculty of Engineering of McGill University for financial support through the MEDA scholarship program. We wish to acknowledge Compute Canada for computational resources and technical support.

References

[1] N. A. Yaraghi, N. Guarín-Zapata, L. K. Grunenfelder, E. Hintsala, S. Bhowmick, J. M. Hiller, M. Betts, E. L. Principe, J.-Y. Jung, L. Sheppard, et al., A sinusoidally architected helicoidal biocomposite, Advanced Materials 28 (32) (2016) 6835–6844.

[2] L. Mencattelli, S. T. Pinho, Herringbone-bouligand cfrp structures: A new tailorable damage-tolerant solution for damage containment and reduced delaminations, Composites Science and Technology 190 (2020) 108047.

[3] H. W. Meyer, W. Richter, G. Brezesinski, Convex-concave curvatures in bilayers of dipalmitoylphosphatidylcholine and cholesterol induced by amphotericin b/deoxycholate after prolonged storage, Biochimica et Biophysica Acta (BBA)-Biomembranes 1190 (1) (1994) 9–19.

[4] J. Tocanne, P. T. Ververgaert, A. Verkleij, L. Van Deenen, A monolayer and freeze-etching study of charged phospholipids ii. ionic properties of mixtures of phosphatidylglycerol and lysylphosphatidylglycerol, Chemistry and physics of lipids 12 (3) (1974) 220–231.

[5] V. V. Yuzhakov, P. V. Takhistov, A. E. Miller, H.-C. Chang, Pattern selection during electropolishing due to double-layer effects, Chaos: An Interdisciplinary Journal of Nonlinear Science 9 (1) (1999) 62–77.

[6] L. Feng, Y. Zhang, J. Xi, Y. Zhu, N. Wang, F. Xia, L. Jiang, Petal effect: a superhydrophobic state with high adhesive force, Langmuir 24 (8) (2008) 4114–4119.

[7] Y. Shukla, M. Sharma, 'egg-carton'shaped plausible organo-sedimentary structures from the archaean dharwar craton, india, International Journal of Earth Sciences 109 (3) (2020) 931–932.

[8] R. Goetz, W. Helfrich, The egg carton: theory of a periodic superstructure of some lipid membranes, Journal de Physique II 6 (2) (1996) 215–223.

[9] G. Brown, A. Chakrabarti, Ordering of block copolymer melts in confined geometry, The Journal of chemical physics 102 (3) (1995) 1440–1448.

[10] W. Yip, C. Welch, G. H. Mehl, T. D. Wilkinson, A cholesteric liquid crystal device having stable uniform lying helix structure, Journal of Molecular Liquids 299 (2020) 112141.

[11] B. Outram, S. Elston, R. Tuffin, S. Siemianowski, B. Snow, The use of mould-templated surface structures for high-quality uniform-lying-helix liquid-crystal alignment, Journal of Applied Physics 113 (21) (2013) 213111.

[12] A. D. Rey, Liquid crystal models of biological materials and processes, Soft Matter 6 (2010) 3402–3429.

[13] A. C. Neville, Biology of Fibrous Composites: Development beyond the Cell Membrane, Cambridge University Press, 1993.

[14] B. D. Wilts, H. M. Whitney, B. J. Glover, U. Steiner, S. Vignolini, Natural helicoidal structures: Morphology, self-assembly and optical properties, Materials Today: Proceedings 1 (2014) 177 – 185.

[15] B. Natarajan, J. W. Gilman, Bioinspired bouligand cellulose nanocrystal composites: a review of mechanical properties, Philosophical Transactions of the Royal Society A: Mathematical, Physical and Engineering Sciences 376 (2112) (2018) 20170050.

[16] A. P. Almeida, J. P. Canejo, S. N. Fernandes, C. Echeverria, P. L. Almeida, M. H. Godinho, Cellulose-based biomimetics and their applications, Advanced Materials 30 (19) (2018) 1703655.

[17] Y. Bouligand, Twisted fibrous arrangements in biological materials and cholesteric mesophases, Tissue and Cell 4 (2) (1972) 189–217.

[18] M.-M. Giraud-Guille, Twisted plywood architecture of collagen fibrils in human compact bone osteons, Calcified tissue international 42 (3) (1988) 167–180.

[19] M. Mitov, Cholesteric liquid crystals in living matter, Soft Matter 13 (23) (2017) 4176–4209.

[20] A. P. Almeida, J. P. Canejo, P. L. Almeida, M. H. Godinho, Cholesteric-type cellulosic structures: from plants to applications, Liquid Crystals 46 (13-14) (2019) 1937–1949.

[21] M. Mitov, N. Dessaud, Going beyond the reflectance limit of cholesteric liquid crystals, Nature materials 5 (5) (2006) 361–364.

[22] A. Scarangella, V. Soldan, M. Mitov, Biomimetic design of iridescent insect cuticles with tailored, self-organized cholesteric patterns, Nature communications 11 (1) (2020) 1–10.

[23] I. Dierking, A. Martins Figueiredo Neto, Novel trends in lyotropic liquid crystals, Crystals 10 (7) (2020) 604.

[24] J. P. Lagerwall, C. Schütz, M. Salajkova, J. Noh, J. H. Park, G. Scalia, L. Bergström, Cellulose nanocrystal-based materials: from liquid crystal self-assembly and glass formation to multifunctional thin films, NPG Asia Materials 6 (1) (2014) e80.

[25] C. Honorato-Rios, J. Bruckner, C. Schütz, S. Wagner, Z. Tosheva, L. Bergström, J. P. Lagerwall, Cholesteric liquid crystal formation in suspensions of cellulose nanocrystals, in: Liquid Crystals with Nano and Microparticles, World Scientific, 2017, pp. 871–897.

[26] A. D. Rey, E. E. Herrera-Valencia, Liquid crystal models of biological materials and silk spinning, Biopolymers 97 (6) (2012) 374–396.

[27] V. Sharma, M. Crne, J. O. Park, M. Srinivasarao, Bouligand structures underlie circularly polarized iridescence of scarab beetles: A closer view, Materials Today: Proceedings 1 (161-171) (2014) 12.

[28] G. De Luca, A. Rey, Monodomain and polydomain helicoids in chiral liquid-crystalline phases and their biological analogues, The European Physical Journal E 12 (2) (2003) 291–302.

[29] G. De Luca, A. D. Rey, Chiral front propagation in liquid-crystalline materials: formation of the planar monodomain twisted plywood architecture of biological fibrous composites, Physical Review E 69 (1) (2004) 011706.

[30] Y. K. Murugesan, A. D. Rey, Modeling textural processes during self-assembly of plant-based chiral-nematic liquid crystals, Polymers 2 (4) (2010) 766–785.

[31] A. D. Rey, E. Herrera-Valencia, Y. K. Murugesan, Structure and dynamics of biological liquid crystals, Liquid Crystals 41 (3) (2014) 430–451.

[32] Y. Bouligand, Liquid crystals and biological morphogenesis: Ancient and new questions, Comptes Rendus Chimie 11 (3) (2008) 281–296.

[33] P. Rofouie, D. Pasini, A. Rey, Tunable nano-wrinkling of chiral surfaces: Structure and diffraction optics, The Journal of chemical physics 143 (11) (2015) 09B613_1.

[34] B. A. Kheireddin, T. C. Williams, M. Akbulut, Tribological properties of femur–tibia articulation of lubber grasshopper, Tribology international 50 (2012) 76–81.

[35] M. Shariatzadeh, D. Grecov, Aqueous suspensions of cellulose nanocrystals as water-based lubricants, Cellulose 26 (7) (2019) 4665–4677.

[36] A. Velasco-Hogan, J. Xu, M. A. Meyers, Additive manufacturing as a method to design and optimize bioinspired structures, Advanced Materials 30 (52) (2018) 1800940.

[37] S. A. Khadem, A. D. Rey, Thermodynamic modelling of acidic collagenous solutions: from free energy contributions to phase diagrams, Soft matter 15 (8) (2019) 1833–1846.

[38] S. A. Khadem, A. Rey, Theoretical platform for liquid-crystalline self-assembly of collagen-based biomaterials, Frontiers in Physics 7 (2019) 88.

[39] O. F. A. Gutierrez, A. D. Rey, Biological plywood film formation from para-nematic liquid crystalline organization, Soft Matter 13 (44) (2017) 8076–8088.

[40] P. Rofouie, D. Pasini, A. D. Rey, Morphology of elastic nematic liquid crystal membranes, Soft matter 13 (32) (2017) 5366–5380.

[41] J. Rodriguez-Hernandez, Wrinkled interfaces: Taking advantage of surface instabilities to pattern polymer surfaces, Progress in Polymer Science 42 (2015) 1–41.

[42] C. González-Henríquez, M. S. Vallejos, J. Rodríguez-Hernández, Introduction to surface instabilities and wrinkle formation, in: Wrinkled Polymer Surfaces, Springer, 2019, pp. 3–18.

[43] H. M. Whitney, M. Kolle, P. Andrew, L. Chittka, U. Steiner, B. J. Glover, Floral iridescence, produced by diffractive optics, acts as a cue for animal pollinators, Science 323 (5910) (2009) 130–133.

[44] A. D. Rey, Capillary models for liquid crystal fibers, membranes, films, and drops, Soft Matter 3 (11) (2007) 1349–1368.

[45] A.-G. Cheong, A. D. Rey, Cahn-hoffman capillarity vector thermodynamics for liquid crystal interfaces, Physical Review E 66 (2) (2002) 021704.

[46] A.-G. Cheong, A. D. Rey, Cahn–hoffman capillarity vector thermodynamics for curved liquid crystal interfaces with applications to fiber instabilities, The Journal of chemical physics 117 (10) (2002) 5062–5071.

[47] Z. Wang, P. Servio, A. D. Rey, Mechanogeometry of nanowrinkling in cholesteric liquid crystal surfaces, Physical Review E 101 (6) (2020) 062705.

[48] Z. Wang, P. Rofouie, A. D. Rey, Surface anchoring effects on the formation of two-wavelength surface patterns in chiral liquid crystals, Crystals 9 (4) (2019) 190.

[49] P. Rofouie, Z. Wang, A. Rey, Two-wavelength wrinkling patterns in helicoidal plywood surfaces: imprinting energy landscapes onto geometric landscapes, Soft Matter 14 (25) (2018) 5180–5185.

[50] R. Meister, H. Dumoulin, M.-A. Hallé, P. Pieranski, The anchoring of a cholesteric liquid crystal at the free surface, Journal de Physique II 6 (6) (1996) 827–844.

[51] J. E. Kirkwood, G. G. Fuller, Liquid crystalline collagen: a self-assembled morphology for the orientation of mammalian cells, Langmuir 25 (5) (2009) 3200–3206.

[52] D. Liu, C. W. Bastiaansen, J. M. den Toonder, D. J. Broer, Photoswitchable surface topologies in chiral nematic coatings, Angewandte Chemie International Edition 51 (4) (2012) 892–896.

[53] B. Terris, R. Twieg, C. Nguyen, G. Sigaud, H. Nguyen, Force microscopy of chiral liquid-crystal surfaces, EPL (Europhysics Letters) 19 (2) (1992) 85.

[54] S. N. Fernandes, Y. Geng, S. Vignolini, B. J. Glover, A. C. Trindade, J. P. Canejo, P. L. Almeida, P. Brogueira, M. H. Godinho, Structural color and iridescence in transparent sheared cellulosic films, Macromolecular Chemistry and Physics 214 (1) (2013) 25–32.

[55] M. Antonietti, C. Göltner, Superstructures of functional colloids: chemistry on the nanometer scale, Angewandte Chemie International Edition in English 36 (9) (1997) 910–928.

[56] R. Goetz, W. Helfrich, The egg carton: theory of a periodic superstructure of some lipid membranes, Journal de Physique II 6 (2) (1996) 215–223.

[57] Z. Tu, J. Liu, Y. Xie, Z.-c. Ou-yang, Geometric Methods in Elastic Theory of Membranes in Liquid Crystal Phases, Vol. 2, World Scientific, 2017.

[58] B. Outram, S. Elston, Spontaneous and stable uniform lying helix liquid-crystal alignment, Journal of Applied Physics 113 (4) (2013) 043103.

[59] H. K. Bisoyi, T. J. Bunning, Q. Li, Stimuli-driven control of the helical axis of self-organized soft helical superstructures, Advanced Materials 30 (25) (2018) 1706512.

[60] K.-S. Park, J.-H. Baek, Y.-J. Lee, J.-H. Kim, C.-J. Yu, Effects of pretilt angle and anchoring energy on alignment of uniformly lying helix mode, Liquid Crystals 43 (9) (2016) 1184–1189.

[61] A. D. Rey, M. M. Denn, Dynamical phenomena in liquid-crystalline materials, Annual Review of Fluid Mechanics 34 (1) (2002) 233–266.

[62] A. D. Rey, E. E. Herrera-Valencia, O. F. Aguilar Gutierrez, Liquid crystalline polymers: Structure and dynamics, Liquid Crystalline Polymers (2020) 273–313.

[63] C. Echeverria, P. L. Almeida, O. F. Aguilar Gutierrez, A. D. Rey, M. H. Godinho, Two negative minima of the first normal stress difference in a cellulose-based cholesteric liquid crystal: Helix uncoiling, Journal of Polymer Science Part B: Polymer Physics 55 (10) (2017) 821–830.

[64] A. D. Rey, Generalized cholesteric permeation flows, Physical Review E 65 (2) (2002) 022701.

[65] A. D. Rey, Simple shear and small amplitude oscillatory rectilinear shear permeation flows of cholesteric liquid crystals, Journal of Rheology 46 (1) (2002) 225–240.

[66] S. A. Chang, D. G. Gray, The surface tension of aqueous hydroxypropyl cellulose solutions, Journal of Colloid and Interface Science 67 (2) (1978) 255–265.

[67] S. A. Khadem, M. Bagnani, R. Mezzenga, A. D. Rey, Relaxation dynamics in bio-colloidal cholesteric liquid crystals confined to cylindrical geometry, Nature communications 11 (1) (2020) 1–10.

[68] A. D. Rey, Marangoni flow in liquid crystal interfaces, The Journal of chemical physics 110 (19) (1999) 9769–9770.

[69] O. L. Schoenborn, Phase-ordering kinetics on curved surfaces, Ph.D. thesis, University of Toronto (1994).

[70] J. Fournier, Nontopological saddle-splay and curvature instabilities from anisotropic membrane inclusions, Physical review letters 76 (23) (1996) 4436.